
# Mutation-induced changes of transmembrane pore size revealed by combined ion-channel conductance and single vesicle permeabilization analyses

Eneko Largo, Douglas P. Gladue, Johana Torralba, Vicente M. Aguilella, Antonio Alcaraz, Manuel V. Borca, José L. Nieva

PII: S0005-2736(18)30012-9
DOI: https://doi.org/10.1016/j.bbamem.2018.01.012
Reference: BBAMEM 82682

To appear in:

Received date: 2 October 2017
Revised date: 25 November 2017
Accepted date: 4 January 2018

Please cite this article as: Eneko Largo, Douglas P. Gladue, Johana Torralba, Vicente M. Aguilella, Antonio Alcaraz, Manuel V. Borca, José L. Nieva , Mutation-induced changes of transmembrane pore size revealed by combined ion-channel conductance and single vesicle permeabilization analyses. The address for the corresponding author was captured as affiliation for all authors. Please check if appropriate. Bbamem(2018), https://doi.org/10.1016/j.bbamem.2018.01.012

# Mutation-induced changes of transmembrane pore size revealed by combined ion-channel conductance and single vesicle permeabilization analyses.

Eneko Largo[a], Douglas P. Gladue[b], Johana Torralba[a], Vicente M. Aguilella[c], Antonio Alcaraz[c], Manuel V. Borca[b], and José L. Nieva[a*]

[a]Biofisika Institute (CSIC, UPV/EHU) and Biochemistry and Molecular Biology Department, University of the Basque Country (UPV/EHU), P.O. Box 644, 48080 Bilbao, Spain.

[b]Plum Island Animal Disease Center, ARS, USDA, Greenport, NY 11944, USA.

[c]Laboratory of Molecular Biophysics. Department of Physics. University Jaume I, 12071 Castellón, Spain

*Corresponding author:

E-mail: joseluis.nieva@ehu.es

**Abstract:**

Permeabilization of the Endoplasmic Reticulum (ER) is instrumental in the progression of host-cell infection by many viral pathogens. We have described that permeabilization of ER model membranes by the pore-forming domain of the Classical Swine Fever Virus (CSFV) p7 protein depends on two sequence determinants: the C-terminal transmembrane helix, and the preceding polar loop that regulates its activity. Here, by combining ion-channel activity measurements in planar lipid bilayers with imaging of single Giant Unilamellar Vesicles (GUVs), we demonstrate that point substitutions directed to conserved residues within these regions affect ER-like membrane permeabilization following distinct mechanisms. Whereas the polar loop appeared to be involved in protein insertion and oligomerization, substitution of residues predicted to face the lumen of the pore inhibited large conducting channels (> 1nS) over smaller ones (120 pS). Quantitative analyses of the ER-GUV distribution as a function of the solute size revealed a selective inhibition for the permeation of solutes with sizes larger than 4 kDa, further demonstrating that the mutation targeting the transmembrane helix prevented formation of the large pores. Collectively, our data support the idea that the pore-forming domain of p7 may assemble into finite pores with approximate diameters of 1 and 5 nm. Moreover, the observation that the mutation interfering with formation of the larger pores can hamper virus production without affecting ER localization or homo-oligomerization, suggests prospective strategies to block/attenuate pestiviruses.

**Key words:** pore-forming peptide; membrane permeabilization; ion channel; ER membrane; peptide-lipid interaction

## 1. Introduction

Unregulated pore formation in cell membranes results in the alteration of the ionic homeostasis, the loss of electrochemical gradients and ultimately cell death. Secreted pore-forming proteins or peptides targeting membranes constitute molecular weapons produced by organisms of diverse origin, and are also part of ancestral immune systems, which are functional in defending against pathogen invasion [1-6]. Membrane specificity of pore formation can be in addition exploited as the basis for antibiotic and anti-cancer drug development [7-9]. Thus, unravelling the molecular mechanisms that sustain the formation of permeating pores and govern their functioning in lipid bilayers remains a highly relevant research issue [3, 10-13].

Poration of the plasma membrane and the different components of the endomembrane system is also a significant issue in the cell infection cycle of many viruses. Formation by virally encoded pore-forming proteins (designated as "viroporins"[14]), of poorly-selective, ion-conductive channels has been proved instrumental in uncoating, transport and maturation of viral particles, but can also influence spread and pathogenicity [15, 16]. A conspicuous organelle targeted by viroporins is the Endoplasmic Reticulum (ER) [17]. Besides its taking part in the different stages of viral replication and assembly, permeabilization of this organelle can modulate several viral functions and plays an important role in host cell-death [15, 17]. Thus, ER permeabilization by pore-forming viral products is a biologically relevant phenomenon, but studies addressing the mechanisms of pore formation in ER model membranes are to a great extent missing.

To address this issue, we have recently modelled the ER permeabilization phenomenon combining: (i) membranes that emulated the ER lipid composition; and

(ii) the pore-forming domain of the Classical Swine Fever Virus (CSFV) p7 product [18-20]. In the one hand, even though the ER is the main site of synthesis of sterols and complex sphingolipids, the ER membrane displays only low concentrations of these lipid species at localized sites [21]. Accordingly, the overall ER membrane can be fairly modelled by a combination of its main constituent phospholipids: zwitterionic PC and PE plus the anionic PI mixed in a roughly 5:3:2 molar ratio [21]. On the other hand, CSFV p7 is a small, hydrophobic protein of approximately 60-70 amino acids, which displays membrane-porating activity and forms homo-oligomers that mainly localize to the ER [15, 18, 19, 22]. Large Unilamellar vesicle (LUV) permeability assays mapped the p7 porating domain to its C-terminal transmembrane helix, while the addition of the preceding polar segment conferred pH dependence and sensitivity to channel blockers [19]. These observations were further supported by functional measurements of ion-conducting channel (IC) activity in ER-like planar lipid membranes [20], which confirmed that a sequence combining the polar segment and the C-terminal helix, designated as p7C, comprises the pore-forming domain of the protein.

Here, to gain insights into the mechanisms underlying ER permeabilization by viral products and its potential relation to virulence, we have focused on the effect of point mutations involving strictly conserved residues within the cytosolic loop and transmembrane helix of CSFV p7C [18]. We have followed an unprecedented combined approach to analyze pore formation, namely, IC activity measurements in planar bilayers and determination of the permeabilization degrees of individual vesicles by fluorescence microscopy imaging. Our combinational approach provided evidence sustaining the formation in ER-like membranes of two types of p7C pores with approximate diameters of 1 and 5 nm. Moreover, the observation that a mutation favoring the small pores hampered virus production without affecting ER localization,

points to the large pore structures as potential targets for blocking pestivirus propagation and pathogenicity.

## 2.Materials and Methods

**2.1 Materials** – Synthetic peptides p7C-wt, p7C-FH, and p7C-KK (sequences displayed in Fig 1A) were produced as previously described [18, 19]. Phosphatidylcholine (PC), phospahtidylethanolamine (PE), phospahtidylethanolamine-N-(lissamine rhodamine B sulfonyl) (Rho-PE), and phosphatidylinositol (PI) were purchased from Avanti Polar Lipids (Birmingham, AL, USA). The 8-aminonaphtalene-1,3,6-trisulfonic acid sodium salt (ANTS), p-xylenebis(pyridinium)bromide (DPX), phenol 4-[5-(4-methyl-1-piperazinyl)[2,5'-bi-1H-benzimidazol]-2'-yl]- trihydrochloride (Hoechst 33258), and Alexa Fluor 488 were obtained from Molecular Probes (Junction City, OR, USA). Rabbit polyclonal antibody against GFP (FL) conjugated with horseradish peroxidase (HRP) was obtained from Santa Cruz Biotechnology (Dallas, TX, USA). Plasmid containing mCh-Sec61 beta was a gift from Gia Voeltz (Addgene plasmid # 49155) [23].

**2.2 Monolayer penetration assays** – Penetration into lipid monolayers was measured to compare the capacity of p7 peptides for inserting into membranes that mimic the ER [19]. In brief, maximal changes in surface pressure were monitored as a function of initial surface pressure ($\pi_0$) in a fixed-area circular trough (μTrough S system, Kibron, Helsinki) measuring 2 cm in diameter and with a volume of 1.25 ml. The aqueous phase consisted of 1 ml of 5 mM NaOAc, 100 mM NaCl (pH 5.0). Lipids, dissolved in chloroform, were spread over the surface and the desired $\pi_0$ was attained by changing the amount of lipid applied to the air-water interface. For allowing incorporation into

the monolayer, peptides were injected into the aqueous subphase with a Hamilton microsyringe.

**2.3 Vesicle permeability assays** – ER-like large unilamellar vesicles (LUV) were prepared according to the extrusion method [24]. Vesicle permeabilization was assayed by monitoring the release to the medium of encapsulated fluorescent ANTS (ANTS-DPX assay) [25]. LUV containing 12.5 mM ANTS, 45 mM DPX, 20 mM NaCl and 5 mM Hepes were obtained by separating the unencapsulated material by gel-filtration in a Sephadex G-75 column that was eluted with 5 mM Hepes and 100 mM NaCl (pH 7.4). Internal and external osmolarities were measured in a cryoscopic osmometer (Osmomat 030, Gonotec, Berlin, Germany) and adjusted by adding NaCl. Fluorescence measurements were performed in an SLM Aminco 8100 spectrofluorimeter (Spectronic Instruments, Rochester, NY) by setting the ANTS emission at 520 nm and the excitation at 355 nm. A cutoff filter (470 nm) was placed between the sample and the emission monochromator. The baseline leakage (0%) corresponded to the fluorescence of the vesicles at time 0, while 100% leakage was the fluorescence value obtained after addition of Triton X-100 (0.5% v/v).

**2.4 Planar lipid membranes formation** –. Two monolayers were made from 5 mg/ml pentane solutions of lipid mixture buffered with 5 mM NaOAc with 150 mM KCl at both sides of Teflon chambers partitioned by a 15 μm thick Teflon film with 70-100 μm diameter orifices. Planar lipid bilayers were formed by monolayer apposition on the orifices previously treated with a 1% solution of hexadecane in pentane. Protein and peptides dissolved in DMSO were supplemented to the lipid solutions prior to monolayer formation only in one of the chamber sides, the *cis* side. Bilayer formation was directly detected and its thickness can be estimated by capacitance measurements.

**2.5 Channel conductance measurements –** An electric potential was applied using Ag/AgCl electrodes in 2 M KCl, 1.5% agarose bridges assembled within standard 250 µl pipette tips. Potential is defined as positive when it is higher at the side of the protein addition (the *cis* side), while the *trans* side is set to ground. An Axopatch 200B amplifier (Molecular Devices, Sunnyvale, CA) in the voltage-clamp mode was used for measuring the current and applying potential. The membrane chamber and the head stage were isolated from external noise sources with a double metal screen (Amuneal Manufacturing Corp., Philadelphia, PA). For each sample, at least 50 different traces were typically recorded (recording time for each trace was 200 s).

A rough first estimation of pore diameter considered a cylindrical neutral pore. Thus, channel conductance $G$ can be written in terms of solution conductivity $\kappa$, and pore dimensions, according to the following equation:

$$G = \frac{\pi D^2}{4L}\kappa \qquad (1)$$

where $L$ and $D$ stand for length and diameter, respectively.

**2.6 Single vesicle permeabilization** –.For the single vesicle approach, Giant Unilamellar Vesicles (GUVs) made of PC:PE:PI:Rho-PE (50:30:20:0.1 mole ratio) were prepared according to the electroformation method as described in previous works [26, 27]. Confocal fluorescence microscopy images of individual GUVs were obtained in a commercial Nikon D Eclipse TE2000-U fluorescence microscope (Nikon Instruments, Tokyo, Japan). Image processing and analyses were carried out with ImageJ (rsb.info.nih.gov/ij/). Extents of permeabilization were calculated after incubation with Alexa Fluor 488 and 0.2 µM of p7 peptides from the ratio of fluorescence intensity inside and outside each vesicle. Exposure of GUVs to peptide for

30 min or 2 hours rendered essentially the same proportion of vesicles permeabilized, and the same levels of permeabilization per vesicle, therefore indicating that the system was at equilibrium at the times selected for performing the measurements (usually 30 min).

**2.7 Cell expression of recombinant p7** –.For cell expression of GFP-p7 fusion proteins**,** 293T cells (2 x $10^5$ cells) were co-transfected with plasmids encoding GFP-p7 fusions and mCh-Sec61 beta (1 µg each) using calcium phosphate [17]. Under these conditions 70-80% of the cells in the culture were successfully transfected. At 36 h post-transfection, cells were fixed with 4% formaldehyde in phosphate saline buffer (PBS) and incubated with Hoechst dye. Confocal images were acquired on a Leica TCS SP5 II microscope (Leica Microsystems GmbH, Wetzlar, Germany), using a x63 water-immersion objective. For the oligomerization assays, 293T cells (1.5 x $10^6$ cells) were transfected with 10 µg of plasmid encoding GFP-p7 constructs. At 36 h post-transfection, cells were collected in cold PBS, sonicated for 1 min on ice with a probe tip sonicator (MSE Soniprep 150, MSE, UK) and dissolved in SDS-PAGE loading buffer. Oligomers were detected by immunoblot analysis using anti-GFP antibody.

**2.8 Construction of CSFV mutants** –. A full-length infectious clone of the virulent Brescia strain (pBIC) [28] was used as a template to obtain all cDNA as described [18]. pBICv-p7-KK (p7 residues $^{39}$KK$^{40}$ to EE) and pBICv-p7-FH (p7 residues $^{46}$FH$^{47}$ to AA) constructs containing desired mutations in the genomic area encoding for p7 protein were obtained using the QuickChange XL Site-Directed Mutagenesis kit (Stratagene, San Diego, CA). Presence of virus infected cells was detected by immunoperoxidase staining utilizing the CSFV monoclonal antibody WH303 (mAb

WH303) [29] and the Vectastain ABC kit (Vector Laboratories, Burlingame, CA).

## 3.Results

### 3.1 Effect of mutations on monolayer penetration and LUV permeabilization by p7C

The pore-forming domain of CSFV p7 encompasses a transmembrane helix (hydrophobic region 41-67), and the preceding cytosolic loop containing a polar stretch (residues 33-40) [18, 19] (Fig. 1A). In previous work, alignment of p7 employing 37 pestivirus sequences, including those derived from 24 CSFV isolates, highlighted the strict conservation of residues Lys39/Lys40 and Phe-46/His47 [18]. These dipeptides are located within the cytosolic loop and on the hydrophilic face of the pore helix, respectively [18]. Here, we have aimed at elucidating the role of those invariant residues in the pore formation and ion-channel function of p7C-wt, by substituting both Lys39/Lys40 residues to Glu (p7C-KK), and by substituting Phe-46/His47 both with alanines (p7C-FH) (Fig. 1A).

The Figure 1B compares capacities of p7C-wt, p7C-FH and p7C-KK peptides for inserting into ER-like membrane monolayers composed of PC:PE:PI (5:3:2 molar ratio). To estimate penetration capacities, we determined the critical pressures ($\pi_c$-s) for insertion, obtained by extrapolation to $\Delta\pi_i = 0$ (i.e., the surface pressures at which the sequences were excluded from the lipid monolayer) [30]. The parental, p7C-wt, and the p7C-FH mutant were capable of penetrating into ER-like monolayers above surface pressures of unstressed natural membranes ($\pi_c \geq 30$ mN/m, [31]). In sharp contrast, the $\pi_c$ measured for the p7C-KK mutant, ca. 27 mN/m, was below that value, thereby

suggesting a lower capacity to integrate as a component of the membrane monolayer. Moreover, the lower slope observed in this latter sample for the increase in pressure as a function of $\pi_0$, suggests that reduced amounts of peptide could associate with the monolayer.

Comparison of ER-LUV permeabilization (ANTS/DPX release assay) induced by the three p7 peptides is shown in Figure 1C. The parental sequence p7C-wt and the mutant p7C-FH displayed comparable capacities for permeabilizing ER-like liposomes. Consistent with its incapacity for insertion, the p7C-KK peptide showed marginal activity in the ANTS/DPX assay. Thus, overall, results displayed in Figure 1 established a clear distinction between p7-wt and p7-FH in the one hand, and p7-KK on the other, regarding insertion and permeabilization of ER-like membranes. However, bulk permeability measured with the ANTS/DPX assay did not reveal differences between p7-wt and p7-FH mutant.

### 3.2 Effect of mutations on ion-channel activity of p7C

To complement bulk permeability measurements, we next carried out a comparative characterization of IC activity of p7C and derived mutants (Fig 2). Electrophysiological recordings, as those displayed in Figure 2A, demonstrated that each substitution distinctively affected the IC activity measured in ER-like planar bilayers. IC activity of p7C-wt was characterized by "opening" and "closing" events between close current levels (6 ± 1 pA), and occasional jumps to large current levels (> 50 pA). In contrast, p7C-FH exhibited the small changes in conductance (5 ± 1 pA), but large current levels were hardly observed (see also recordings in Fig 2B displayed with a different intensity scale). The statistical analyses of the observed conductance levels displayed on Figure

2C illustrate this point further. Thus, the FH x AA substitution specifically suppressed the high-conductance levels. Finally, IC activity was mostly absent in samples containing the p7C-KK peptide, consistently with the limited membrane insertion detected in the monolayer experiments (Fig. 1B).

The small jumps observed in both, p7C-wt and p7C-FH samples, correspond to channel currents of conductance in the range $G$ = 120-300 pS at the applied voltage (50 mV). Assuming a cylindrical geometry (see Material and Methods), such conductance levels can be attributed to channels with diameters in the range of $d \sim 0.5$ -1 nm. Thus, these pore structures were wide enough to allow release of solutes with the size of the ANTS/DPX fluorescent probe/quencher pair (assumed diameters of 5-8 Å) [32]. Accordingly, p7C-wt and p7C-FH induced comparable levels of ANTS/DPX release from vesicles (see previous Fig 1C).

The origin of the large current levels that are distinctive of the p7C-wt peptide is more difficult to trace. In principle, the electrophysiological experiments do not allow categorical discrimination between two possibilities, namely, the simultaneous opening of several concatenated channels with similar sizes, or the formation of a wider, single-type of channel structure [33, 34]. In the latter case, given that currents between 100 and 350 pA in Figure 2C correspond to conductance values in the range $G$ = 2-7 nS, the estimated channel diameters would span up to $d \approx 5$ nm. Interestingly, the existence of such wide channels could be probed in permeability experiments involving solutes of Stokes' radius between 1 and 3 nm (see below).

### 3.3 Activity of the p7 porating domain assayed in single ER-GUVs

To gain insight into the different mechanisms of permeabilization by the wt and mutant p7 peptides, we complemented ion-channel measurements with a single-vesicle approach based on the use of ER-GUVs (Figs 3 and 4). The confocal micrographs depicted in Figure 3A illustrate the fundamentals of the ER-GUV permeabilization assay. In the general views (top panels), untreated ER-GUVs (CTL), or those treated with p7N peptide representing the N-terminal portion of the viroporin p7 [19], are viewed as dark (empty) spheres surrounded by the orange-labeled lipid bilayer, against a green background containing the permeant Alexa Fluor 488 dye. Incubation with the pore-domain peptide p7C-wt gives rise to green labeling of the internal ER-GUV compartments (arrows), indicating permeabilization of the lipid bilayer to the dye. By analyzing the balance of fluorescence intensity inside and outside the intact vesicles, one can infer the degree of permeabilization (percentage) for a single ER-GUV (bottom panels). Although in the p7C-wt sample the majority of permeabilized vesicles approached 100 % permeabilization (right), some of the vesicles still showed partial filling at equilibrium (center). Whereas total membrane permeabilization occurs through stably assembled pore structures, the partial permeabilization observed in these systems at equilibrium is usually ascribed to the transient destabilization that may occur coupled to peptide insertion.

The quantitative analysis shown in Figure 3B reflects the relative importance of each phenomenon. In those experiments the filling degree of individual ER-GUVs was measured at equilibrium after treatment with p7N or p7C-wt peptides. Consistent with prior ANTS/DPX assays and ion-conductance measurements [20], only p7C-wt incubated at pH 5.0, but not at neutral pH, induced entry of the dye into vesicles, which otherwise maintained their integrity during the process. Finally, peptides bearing the point mutations p7C-KK and p7C-FH reproduced the behavior observed in bulk

ANTS/DPX assays, i.e., no activity in the former case, whereas the activity of the latter was indistinguishable from that of p7C-wt (Fig 3C).

The ER-GUV approach further allowed assessing the formation of pores with distinct dimensions. To that end degrees of vesicle permeabilization were quantitatively determined as a function of the permeative solute size (Fig. 4). Micrographs displayed in Figure 4A compare the observed differences in the filling degree of vesicles when FITC-labeled fluorescent dextrans of 4 or 70 kDa were used to estimate degrees of p7C-wt-induced permeabilization (left and right panels, respectively). The micrographs reveal entry of the low molecular-weight 4kDa dextran (left panels), whereas the larger 70 kDa marker remains outside the vesicles (right panels).

A more detailed quantitative comparison is presented in Figure 4B. Most vesicles treated with p7C-wt were totally permeabilized to 4, 10 and 20 kDa dextrans, whereas a significant reduction in the number of totally permeabilized vesicles was observed for the 70 kDa permeant solute. By comparison, partial permeabilization was overall lower for solutes of all sizes. In contrast, reduction of the total permeabilization levels was already observed for smaller solutes (10 kDa) in the case of the p7C-FH, which resembled in other aspects the wt sequence. As expected, p7C-KK did not show permeabilizing activity for any solute in these assays (not shown).

This point is further illustrated in Figure 4C that compares the percentage of vesicles displaying stable (filling degree>70%) and transient (filling degree: 20-70%) pores (total and partial permeabilization, respectively). Decrease of the total permeabilization levels is observed for the 70 and 4 kDa dextrans in p7C-wt and p7C-FH samples, respectively (left panel). The right panel displays the percentage of vesicles partially

filled (20-70 % permeabilization range). The percentages are in both samples comparable and less significant, and do not seem to depend on the solute size.

In conclusion, the p7C-wt-induced ER-GUV permeabilization appears to evolve primarily mediated by stable pores allowing diffusion of solutes as large as 20 kDa (approximate Stokes' radius of 3.3 nm). This verifies the existence of large pores with diameters of several nanometers as hypothesized in the discussion of Fig 2C (see above). By comparison, the stable pores formed by the peptide bearing the FH x AA mutation seem to be narrower, allowing free diffusion of Alexa Fluor 488 (approximate Stokes' radius of 0.6 nm), limited diffusion of 4kDa dextrans (approximate Stokes' radius of 1.4 nm), and no diffusion of the larger permeative solutes.

### 3.4 Effect of mutations on the distribution/oligomerization of p7 in transfected cells and on virus production

To establish the biological relevance of the studied mutations, we first determined whether they affected the biogenesis and assembly of p7 within the ER (Fig. 5A-C). Confocal microscopy of cells transfected with each of the GFP-p7 constructs was conducted to establish the cell localization of the protein upon synthesis (Fig 5A, B). Expression of the GFP control (i.e., devoid of the membrane anchors) revealed homogeneous cell labeling, including the presence of the fluorescent marker in the nucleus (Fig 5A, top, green label). This was in contrast to the sole labeling of the ER compartment by mCh-Sec61 (Fig 5A, top, red label). Consistent with previously reported data [22], the wild-type construct GFP-p7 co-localized with the ER marker (see also Fig 5B). The FH x AA mutation in the pore domain did not alter significantly the distribution of the protein. Finally, confocal images of the protein bearing the KK x

EE mutation at the cytosolic loop revealed a more diffuse intracellular fluorescent labeling, a pattern resembling cells expressing the GFP control. Accordingly, this latter construct did not co-localize significantly with mCh-Sec61 (Fig 5B).

To test the oligomeric state of the expressed proteins, SDS-PAGE analyses were subsequently performed on extracts of the transfected cells (Fig 5C). Immunoblots probed with the anti-GFP antibody showed bands consistent with the formation of high-order homo-oligomers in cells expressing the GFP-p7 and GFP-p7-FH constructs (arrow). Even though a band consistent with the formation of homo-oligomers was also found in cells expressing the GFP-p7-KK construct, the band corresponding to the higher-order homo-oligomers was absent in these samples. From the results displayed in Figures 5A-C the following conclusion can be drawn: whereas the FH x AA mutation does not alter the biogenesis of the viroporin p7, the KK x EE mutation appears to interfere with insertion into the ER membrane and oligomerization therein.

Finally, to evaluate the effect of the amino acid substitutions $^{39}$KK$^{40}$-EE and $^{46}$FH$^{47}$-AA in the replication of CSFV, two recombinant CSF viruses containing the corresponding amino acid substitutions in the pore-forming domain of p7 were produced using the cDNA infectious clone of the Brescia strain (BICv) as a template. Mutated cDNA infectious clones pBICv-p7-KK and pBICv-p7-FH were developed by site directed mutagenesis.

Infectious RNA was *in vitro* transcribed from each mutated full-length cDNA and used to transfect SK6 cells [18]. Infectious virus was rescued from transfected cells by day 4 post-transfection using the pBIC construct encoding for the parental virus BIC with titers reaching almost $10^7$ $TCID_{50}$/ml. In contrast, after four independent transfection procedures, pBICv-p7-KK and pBICv-p7-FH constructs did not produce

infectious viruses. Real-time RT-PCR analysis of total RNA extracted from cells transfected with pBICv-p7-KK and pBICv-p7-FH constructs revealed genomic RNA replication, (data not shown). In addition, immunohistochemistry analysis of transfected cell monolayers was performed using a monoclonal antibody recognizing CSFV structural glycoprotein E2 (Fig. 5D). As expected, cell monolayers transfected with pBIC-p7 showed a large number of cells expressing massive levels of E2 (right-most panel). Conversely, pBICv-p7-FH transfected cells showed the presence of small and isolated foci of cells expressing structural glycoprotein E2, while there was a complete absence of E2 expression in cells transfected with pBICv-p7-KK construct (mid panels). Attempts to rescue infective virus from cell cultures transfected with either pBICv-p7-KK or pBICv-p7-FH were performed by four successive blind passages in fresh monolayers of SK6 cells. No infectious virus could be detected in any of the four passages for either of the constructs tested. Therefore, residues $^{46}$FH$^{47}$ and $^{39}$KK$^{40}$ in the pore-forming domain of p7 appear to be critical for CSFV replication.

## 4. Discussion

ER permeabilization is a pivotal event required for the progression of the cell replication cycle of many viruses [15, 17]. The CSFV p7 product has been shown to permeabilize ER-like membranes following a lipid-dependent pattern [18, 19], and to localize in the ER upon expression [22], and hence constitutes an optimal model to study this phenomenon. Following strategies described previously [33, 35], in a preceding work we established a minimal channel structure represented by p7C-wt [19]. Those studies pinpointed the polar, cytosolic loop $^{33}$MRDEPIKK$^{40}$, as a regulatory element that conferred pH and inhibitor sensitivity to the pore, and the C-terminal helix $^{41}$WILLLFHAMTNNPVKTITVALLMVSGV$^{67}$ as the actual pore-forming domain. The p7C-wt peptide combined both elements and was simultaneously competent in conducting ions across lipid bilayers mimicking the ER, and in allowing release of small solutes (ANTS/DPX) from ER-LUVs [20]. Motivated by the observation that the invariant residues $^{39}$KK$^{40}$ and $^{46}$FH$^{47}$ were located within these functional regions [18], we sought to analyze the effect of non-conservative KK x EE and FH x AA double substitutions on the pore-forming activity of p7C-wt.

Since the cytosolic loop invests the pore domain of p7 with sensitivity to pH and inhibitors [19, 20], we expected assembly of less regulated pores in membranes be the consequence of substituting the conserved Lys39-Lys40 residues by the negatively charged Glu-Glu dipeptide. However, contrary to our expectations, incorporating the KK x EE mutation in the p7C-KK peptide resulted in defective monolayer penetration and absence of membrane permeabilization (Figs 1-4). These findings suggest that the loop not only regulates permeability but also conditions insertion into ER membranes.

In consonance with this limiting defect, the same mutation resulted in an anomalous distribution and defective homo-oligomerization of p7 upon cell expression (Fig. 5A-C). Interestingly, the suppressing effect of a cognate mutation in HCV p7 has been related to alterations in membrane-topology [36]. From molecular dynamics simulations, it was inferred that the basic residues sitting in the membrane interface could engage electrostatic interactions with negatively charged lipid polar head groups to properly orient the TM helices [33, 37]. Thus, we infer that perturbing the set of interactions between basic Lys-Lys residues and negatively charged PI at the membrane interface, may also result in the inefficient insertion/pore-formation of CSFV p7. Finally, highlighting the crucial role of pore-forming p7 protein in the CSFV replication cycle, the KK x EE mutation also suppressed production of infectious virus (Fig 5D), an observation in line with previous results obtained for p7 of the BVDV pestivirus [38] and our own Ala-scanning mutagenesis [18].

In contrast, the p7C-FH peptide, displayed less capacity for inserting into monolayers than p7C-wt, but retained the membrane-permeabilizing capacity of the parental sequence measured in ANTS/DPX-LUV assays (Fig. 1). However, complementation of these bulk measurements with IC activity and single ER-GUV permeability determinations revealed functional differences between both sequences (Figs. 2-4). Electrophysiogical recordings disclosed two distinct phenotypic traits: co-existence of small and large conductance channels in p7C-wt, and predominance of small apertures in the p7C-FH. Similarly, single-channel recordings of Hepatitis C virus p7 protein by the patch clamp technique revealed distinct conductance values of 35, 57, 120, and 184 pS [33]. It was argued that large conductance levels could represent either insertion of simultaneous channels, or an increase in the number of p7 monomers per channel and hence, a wider current passage. Under our measuring conditions, we observe

comparable conductance levels of 120 pS for both p7C-wt and p7C-FH, which would be compatible with channel sizes allowing release of ANTS/DPX, explaining the similar porating capacities observed in the LUV-based assay. However, in the case of the p7C-wt peptide, these structures co-existed with channels giving rise to higher conductance (> 1 nS) whose origin was uncertain.

To address the origin of the different stages observed in the membrane permeabilization induced by p7C-wt, the process was imaged at the individual vesicle level by fluorescence microscopy of ER-GUVs (Figs 3 and 4). These objects attain cell dimensions and, when applied to permeability assays, the single GUV approach offers several advantages as compared to measurements in bulk (i.e., LUV-based ANTS/DPX assays). Firstly, owing to the fluorescent lipid label, their surrounding lipid bilayer can be readily observed by confocal microscopy, which allows monitoring its overall stability upon treatment with the permeabilizing agent, i.e., one can discern membrane permeabilization through discrete pores vs. lipid bilayer disaggregation by detergent-like mechanisms [3, 10]. Secondly, GUV membranes can be considered as flat planes devoid of curvature stress, i.e., they mimic the conditions of the planar bilayers used in electrophysiological experiments more closely than LUVs. And thirdly, one can discern solute-encapsulation heterogeneities that may arise in the population of permeabilized vesicles, which go unnoticed in bulk measurements [26].

Explicitly, in the case of totally permeabilized GUVs, the open state of the pore lasts enough as to allow the equilibration of the probe with the external medium. Both, p7C-wt and p7C-FH permeabilized ER-GUVs to alexa-488 and 4 kDa-dextran according to this mechanism (Fig. 4B). However, the number of totally permeabilized ER-GUVs dropped for larger dextrans in the case of p7C-FH, but not in the case of p7C-wt (Fig.

4C). This observation suggests that stably opened pores of larger dimensions were only accessible to the wt sequence. On the other hand, the partial permeabilization process seems to be related to transient membrane lesions of the bilayer permeability that do not allow rapid equilibration with the external solution. The fact that the number of ER-GUVs partially permeabilized was marginal in the p7C-wt and p7C-FH samples (Fig 4C), underscores the prevalent role of stable channel-pore structures in mediating IC activity and dye influx into GUVs.

## 5. Conclusions

In conclusion, our IC activity and GUV permeabilization data provide a clear demonstration for assembling channel-pores with distinct aperture widths by the porating domain of p7 CSFV in ER-mimicking membranes. To our best knowledge, this is the first time that electrophysiological and single-vesicle approaches are combined to solve the permeabilization mechanism of a pore-forming product functioning in the context of ER membranes. Notably, the FH x AA mutation favoring small-size pores abrogated virus production without altering the cell distribution or oligomerization degree of p7 upon expression (Fig. 5). Further research efforts will be required to get insight into the distinct physiological roles of the p7C capacity to form pores of different dimensions, and we foresee that the FH x AA mutation described in this work may provide a useful tool in the context of cell infection by pestiviruses. It is tempting to speculate that manipulating pore-forming function of p7 by mutagenesis may provide in the future new approaches to vaccine and anti-viral development to treat pestivirus infections.

**Acknowledgements**

This study was in part supported by the Agricultural Research Service of the US (ARS-USDA Project 8064-32000- 056-18S to EL and JLN) and the Basque Government (Project IT838-13 to JLN). Financial support from the Ministry of Economy and Competitiveness of Spain (projects no. FIS2013-40473-P and FIS2016-75257-P), and Universitat Jaume I (project no. P1.1B2015-28) is also acknowledged.

**References:**

[1] D.M. Ojcius, J.D. Young, Cytolytic pore-forming proteins and peptides: is there a common structural motif?, Trends Biochem Sci, 16 (1991) 225-229.

[2] E. Gouaux, Channel-forming toxins: tales of transformation, Curr Opin Struct Biol, 7 (1997) 566-573.

[3] Y. Shai, Mechanism of the binding, insertion and destabilization of phospholipid bilayer membranes by alpha-helical antimicrobial and cell non-selective membrane-lytic peptides, Biochim Biophys Acta, 1462 (1999) 55-70.

[4] M.W. Parker, S.C. Feil, Pore-forming protein toxins: from structure to function, Prog Biophys Mol Biol, 88 (2005) 91-142.

[5] C.H. Wang, W.G. Wu, Amphiphilic beta-sheet cobra cardiotoxin targets mitochondria and disrupts its network, FEBS Lett, 579 (2005) 3169-3174.

[6] G. Anderluh, J.H. Lakey, Disparate proteins use similar architectures to damage membranes, Trends Biochem Sci, 33 (2008) 482-490.

[7] M. Mathew, R.S. Verma, Humanized immunotoxins: a new generation of immunotoxins for targeted cancer therapy, Cancer Sci, 100 (2009) 1359-1365.

[8] M.L. Mangoni, Y. Shai, Short native antimicrobial peptides and engineered ultrashort lipopeptides: similarities and differences in cell specificities and modes of action, Cell Mol Life Sci, 68 (2011) 2267-2280.

[9] W.C. Wimley, K. Hristova, Antimicrobial peptides: successes, challenges and unanswered questions, J Membr Biol, 239 (2011) 27-34.

[10] W.C. Wimley, Describing the mechanism of antimicrobial peptide action with the

interfacial activity model, ACS Chem Biol, 5 (2010) 905-917.

[11] V.M. Aguilella, M. Queralt-Martin, M. Aguilella-Arzo, A. Alcaraz, Insights on the permeability of wide protein channels: measurement and interpretation of ion selectivity, Integr Biol (Camb), 3 (2011) 159-172.

[12] U. Ros, A.J. Garcia-Saez, More Than a Pore: The Interplay of Pore-Forming Proteins and Lipid Membranes, J Membr Biol, 248 (2015) 545-561.

[13] N. Rojko, M. Dalla Serra, P. Macek, G. Anderluh, Pore formation by actinoporins, cytolysins from sea anemones, Biochim Biophys Acta, 1858 (2016) 446-456.

[14] M.E. Gonzalez, L. Carrasco, Viroporins, FEBS Lett, 552 (2003) 28-34.

[15] J.L. Nieva, V. Madan, L. Carrasco, Viroporins: structure and biological functions, Nat Rev Microbiol, 10 (2012) 563-574.

[16] J.L. Nieto-Torres, C. Verdia-Baguena, C. Castano-Rodriguez, V.M. Aguilella, L. Enjuanes, Relevance of Viroporin Ion Channel Activity on Viral Replication and Pathogenesis, Viruses, 7 (2015) 3552-3573.

[17] M.S. Ravindran, P. Bagchi, C.N. Cunningham, B. Tsai, Opportunistic intruders: how viruses orchestrate ER functions to infect cells, Nat Rev Microbiol, 14 (2016) 407-420.

[18] D.P. Gladue, L.G. Holinka, E. Largo, I. Fernandez Sainz, C. Carrillo, V. O'Donnell, R. Baker-Branstetter, Z. Lu, X. Ambroggio, G.R. Risatti, J.L. Nieva, M.V. Borca, Classical swine fever virus p7 protein is a viroporin involved in virulence in swine, J Virol, 86 (2012) 6778-6791.

[19] E. Largo, D.P. Gladue, N. Huarte, M.V. Borca, J.L. Nieva, Pore-forming activity of pestivirus p7 in a minimal model system supports genus-specific viroporin function, Antiviral Res, 101 (2014) 30-36.

[20] E. Largo, C. Verdia-Baguena, V.M. Aguilella, J.L. Nieva, A. Alcaraz, Ion channel

activity of the CSFV p7 viroporin in surrogates of the ER lipid bilayer, Biochim Biophys Acta, 1858 (2016) 30-37.

[21] G. van Meer, D.R. Voelker, G.W. Feigenson, Membrane lipids: where they are and how they behave, Nat Rev Mol Cell Biol, 9 (2008) 112-124.

[22] H.C. Guo, S.Q. Sun, D.H. Sun, Y.Q. Wei, J. Xu, M. Huang, X.T. Liu, Z.X. Liu, J.X. Luo, H. Yin, D.X. Liu, Viroporin activity and membrane topology of classic swine fever virus p7 protein, The international journal of biochemistry & cell biology, 45 (2013) 1186-1194.

[23] N. Zurek, L. Sparks, G. Voeltz, Reticulon short hairpin transmembrane domains are used to shape ER tubules, Traffic, 12 (2011) 28-41.

[24] M.J. Hope, M.B. Bally, G. Webb, P.R. Cullis, Production of large unilamellar vesicles by a rapid extrusion procedure: characterization of size distribution, trapped volume and ability to maintain a membrane potential, Biochimica et biophysica acta, 812 (1985) 55-65.

[25] H. Ellens, J. Bentz, F.C. Szoka, H+- and Ca2+-induced fusion and destabilization of liposomes, Biochemistry, 24 (1985) 3099-3106.

[26] B. Apellaniz, J.L. Nieva, P. Schwille, A.J. Garcia-Saez, All-or-none versus graded: single-vesicle analysis reveals lipid composition effects on membrane permeabilization, Biophys J, 99 (2010) 3619-3628.

[27] B. Apellaniz, A.J. García-Sáez, N. Huarte, R. Kunert, K. Vorauer-Uhl, H. Katinger, P. Schwille, J.L. Nieva, Confocal microscopy of giant vesicles supports the absence of HIV-1 neutralizing 2F5 antibody reactivity to plasma membrane phospholipids, FEBS Lett, 584 (2010) 1591-1596.

[28] G.R. Risatti, M.V. Borca, G.F. Kutish, Z. Lu, L.G. Holinka, R.A. French, E.R. Tulman, D.L. Rock, The E2 glycoprotein of classical swine fever virus is a virulence determinant in swine, J Virol, 79 (2005) 3787-3796.

[29] C. Terpstra, R. Woortmeyer, S.J. Barteling, Development and properties of a cell culture produced vaccine for hog cholera based on the Chinese strain, DTW. Deutsche tierarztliche Wochenschrift, 97 (1990) 77-79.

[30] R. Maget-Dana, The monolayer technique: a potent tool for studying the interfacial properties of antimicrobial and membrane-lytic peptides and their interactions with lipid membranes, Biochim Biophys Acta, 1462 (1999) 109-140.

[31] D. Marsh, Lateral pressure profile, spontaneous curvature frustration, and the incorporation and conformation of proteins in membranes, Biophys J, 93 (2007) 3884-3899.

[32] J.M. Rausch, J.R. Marks, R. Rathinakumar, W.C. Wimley, Beta-sheet pore-forming peptides selected from a rational combinatorial library: mechanism of pore formation in lipid vesicles and activity in biological membranes, Biochemistry, 46 (2007) 12124-12139.

[33] R. Montserret, N. Saint, C. Vanbelle, A.G. Salvay, J.P. Simorre, C. Ebel, N. Sapay, J.G. Renisio, A. Bockmann, E. Steinmann, T. Pietschmann, J. Dubuisson, C. Chipot, F. Penin, NMR structure and ion channel activity of the p7 protein from hepatitis C virus, J Biol Chem, 285 (2010) 31446-31461.

[34] A. Premkumar, L. Wilson, G.D. Ewart, P.W. Gage, Cation-selective ion channels formed by p7 of hepatitis C virus are blocked by hexamethylene amiloride, FEBS Lett, 557 (2004) 99-103.

[35] V. Madan, S. Sanchez-Martinez, N. Vedovato, G. Rispoli, L. Carrasco, J.L. Nieva, Plasma membrane-porating domain in poliovirus 2B protein. A short peptide mimics viroporin activity, J Mol Biol, 374 (2007) 951-964.

[36] E. Steinmann, F. Penin, S. Kallis, A.H. Patel, R. Bartenschlager, T. Pietschmann, Hepatitis C virus p7 protein is crucial for assembly and release of infectious virions, Plos Pathogens, 3 (2007) 962-971.

[37] D.E. Chandler, F. Penin, K. Schulten, C. Chipot, The p7 protein of hepatitis C

virus forms structurally plastic, minimalist ion channels, PLoS computational biology, 8 (2012) e1002702.

[38] T. Harada, N. Tautz, H.J. Thiel, E2-p7 region of the bovine viral diarrhea virus polyprotein: processing and functional studies, J Virol, 74 (2000) 9498-9506.

**Figure captions**

**Fig 1: Effects of mutations on p7C insertion into membranes and LUV permeabilization.** A) Designation and sequences of CSFV p7 peptides used in the analysis. The ribbon and helix displayed below span the sequences of the polar cytosolic loop and the C-terminal transmembrane helix of p7, respectively. B) Insertion into ER-like lipid monolayers. Maximum increase in surface pressure induced by p7C-wt, p7C-FH or p7C-KK peptides (black, blue and red, respectively), measured as a function of the initial surface pressure of the phospholipid monolayer. The dotted line at 30 mN/m marks the pressure of an unstressed membrane. The critical pressures for insertion ($\pi_c$-s) of each peptide are indicated in the panel. C) Comparison of leakage levels induced by increasing peptide doses in the ANTS/DPX assay. The plotted values correspond to extents of leakage measured 200 s after p7C-wt, p7C-FH or p7C-KK peptide addition to ER-LUVs (black, blue and red, respectively).

**Fig 2: Effects of p7 mutations on ion-channel activity** A) Typical current recordings measured in 150 mM KCl, pH 5.0 at a potential of -50 mV, after the addition of p7C-wt, p7C-FH or p7C-KK to ER-like lipid bilayers. B) To illustrate the different magnitude of current levels seen in the experiments, traces of the p7C-wt and p7C-FH ion channel activity have been displayed with a different intensity scale. C) Histograms of the current levels recorded for p7C-wt and p7C-FH (left and right panels, respectively).

**Fig 3: Single ER-GUV permeabilization induced by p7 peptides**. A) Top: micrographs depict Rho-PE-labeled ER-GUVs (orange circumferences) immersed in a solution containing Alexa Fluor 488 (green background). Samples correspond to control-untreated ER-GUVs (left), or ER-GUVs treated with p7N or p7C-wt (center and right panels, respectively). The red arrows point to permeabilized vesicles in the latter sample. Bottom: single ER-GUVs treated with p7C-wt displaying different levels of permeabilization to Alexa Fluor 488. B) Distribution of ER-GUVs according to their permeabilization level after treatment with p7N or p7C-wt at pH 5.0, or p7C-wt at pH 7.4. C) Effect of the mutations on permeabilization of the ER-GUVs measured at pH 5.0. Horizontal scales in panels B and C, chosen arbitrarily to show the distribution of points.

**Fig 4: ER-GUV permeabilization as a function of the solute size.** A) Micrographs compare p7C-wt-induced permeabilization to dextrans of 4 and 70 kDa (left and right

panels, respectively). B) ER-GUV distribution according to the percentage of permeabilization per vesicle. Samples were treated with the p7 peptides as indicated in the panels, and percentages of entry in single vesicles calculated for the different solutes. C) Percentages of vesicles permeabilized via stable or transient pores as a function of the solute size (left and right panels, respectively). The threshold by which permeabilized GUVs (>20% filling) were considered as totally (filling degree >70%) or partially (filling degree <70%) permeabilized was chosen attending to the data-point distribution.

**Fig 5: Effects of the mutations on the distribution/oligomerization state of recombinant p7 within cells and on virus production.** A) Distribution of p7 and its mutants by confocal microscopy. The cells co-transfected with GFP-p7 constructs and the ER marker mCh-Sec61 were fixed and stained with Hoechst. The panels depict examples of individual cells co-expressing GFP constructs and mCh-Sec61. Scalebars represent 10 µm. The control GFP devoid of membrane anchors labelled the complete cell (top panel). GFP-p7 and GFP-p7-FH were excluded from the nucleus and co-localized with mCh-Sec61 (mid top and bottom panels, respectively). GFP-p7-KK (bottom panel), produced a pattern comparable to that obtained after expression of GFP control. B) Co-localization of mCh-Sec6 and GFP in the samples as calculated with the ImageJ plugin Coloc 2 program (http://imagej.net/Coloc_2). Measurements were carried out in at least 6 cells as those displayed in the previous panel. Bars represent mean values ± SE. C) Homo-oligomerization in cells transfected with the GFP constructs. Cell extracts were applied to SDS-PAGE and GFP detected using Western blotting. The arrow marks the band corresponding to high-order homo-oligomers. D) CSFV protein expression in SK6 cultures transfected with infectious clones encoding for p7 mutants and parental BICv. Detection of CSFV E2 protein was done by immunocytochemistry in SK6 cells transfected with recombinant constructs pBICv-p7-KK and pBICv-p7-FH. SK6 cells were transfected with either mutant construct or with infectious clone encoding for parental wild type virus (pBIC-p7). Four days after transfection monolayers were ethanol:acetone fixed and stained with monoclonal antibody WH303 which specifically recognize CSFV structural glycoprotein E2.

**Highlights:**

- We have analyzed ion-channel activity and single GUV permeabilization by CSFV p7
- The data support the formation of p7 pores with approximate diameters of 1 and 5 nm
- A mutation results in loss of large ion-conducting channels and restricted pore size
- Manipulation of p7 pores may provide new strategies to attenuate pestivirus particles

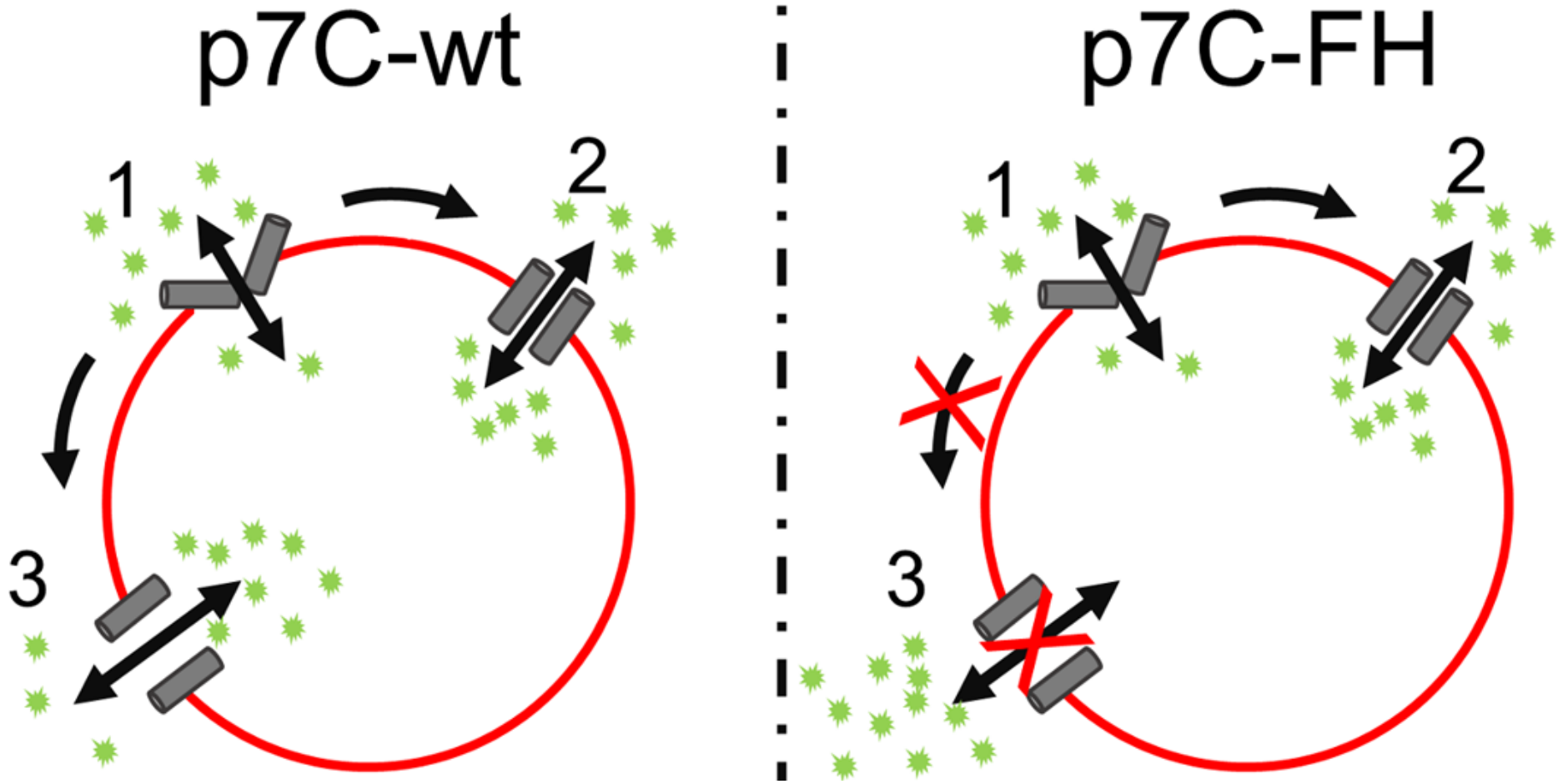


Graphics Abstract

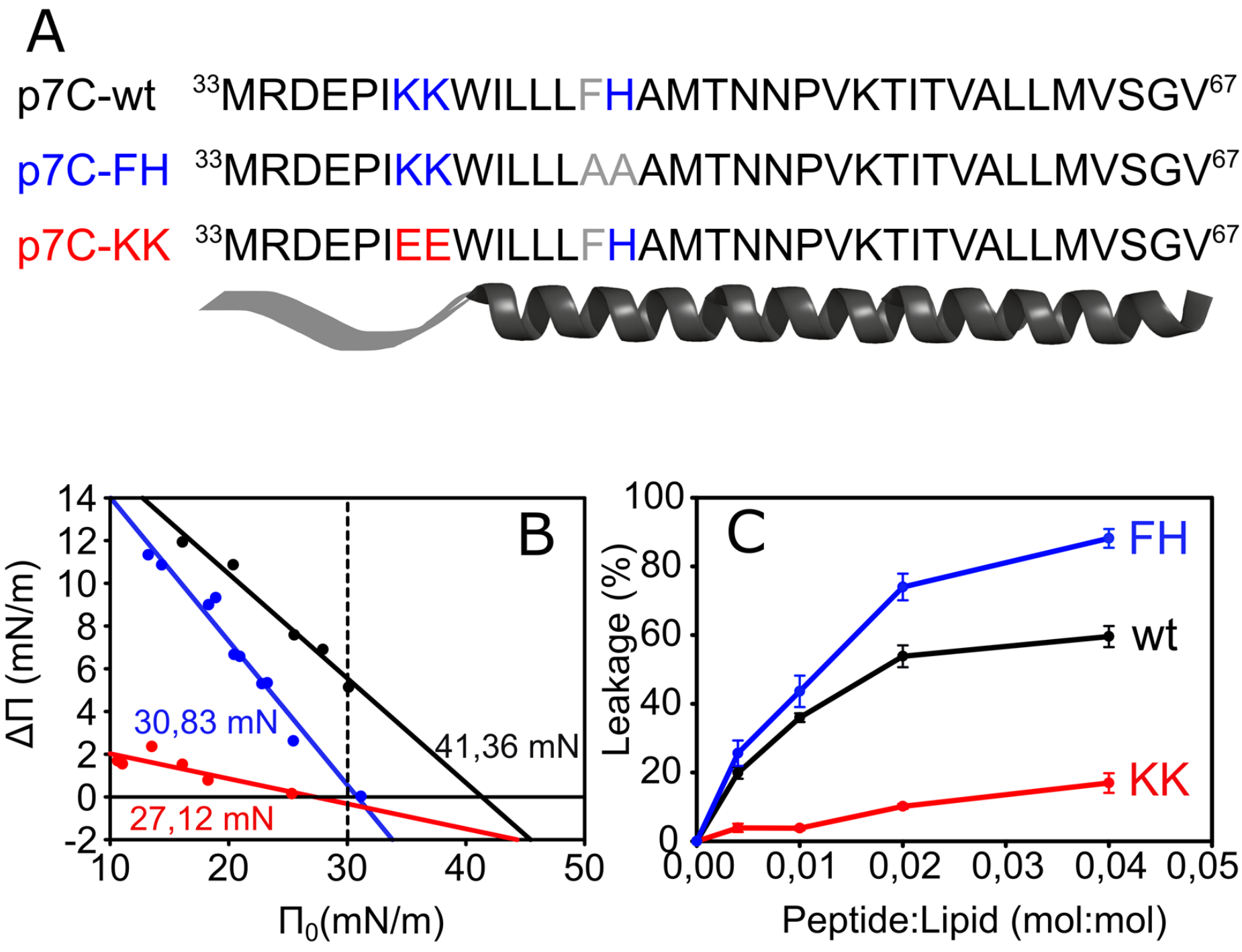
A
p7C-wt 33MRDEPIKKWILLLFHAMTNNPVKTITVALLMVSGV67
p7C-FH 33MRDEPIKKWILLLAAAMTNNPVKTITVALLMVSGV67
p7C-KK 33MRDEPIEEWILLLFHAMTNNPVKTITVALLMVSGV67
B
ΔΠ (mN/m)
Π0(mN/m)
30,83 mN
41,36 mN
27,12 mN
C
Leakage (%)
Peptide:Lipid (mol:mol)
FH
wt
KK

Figure 1

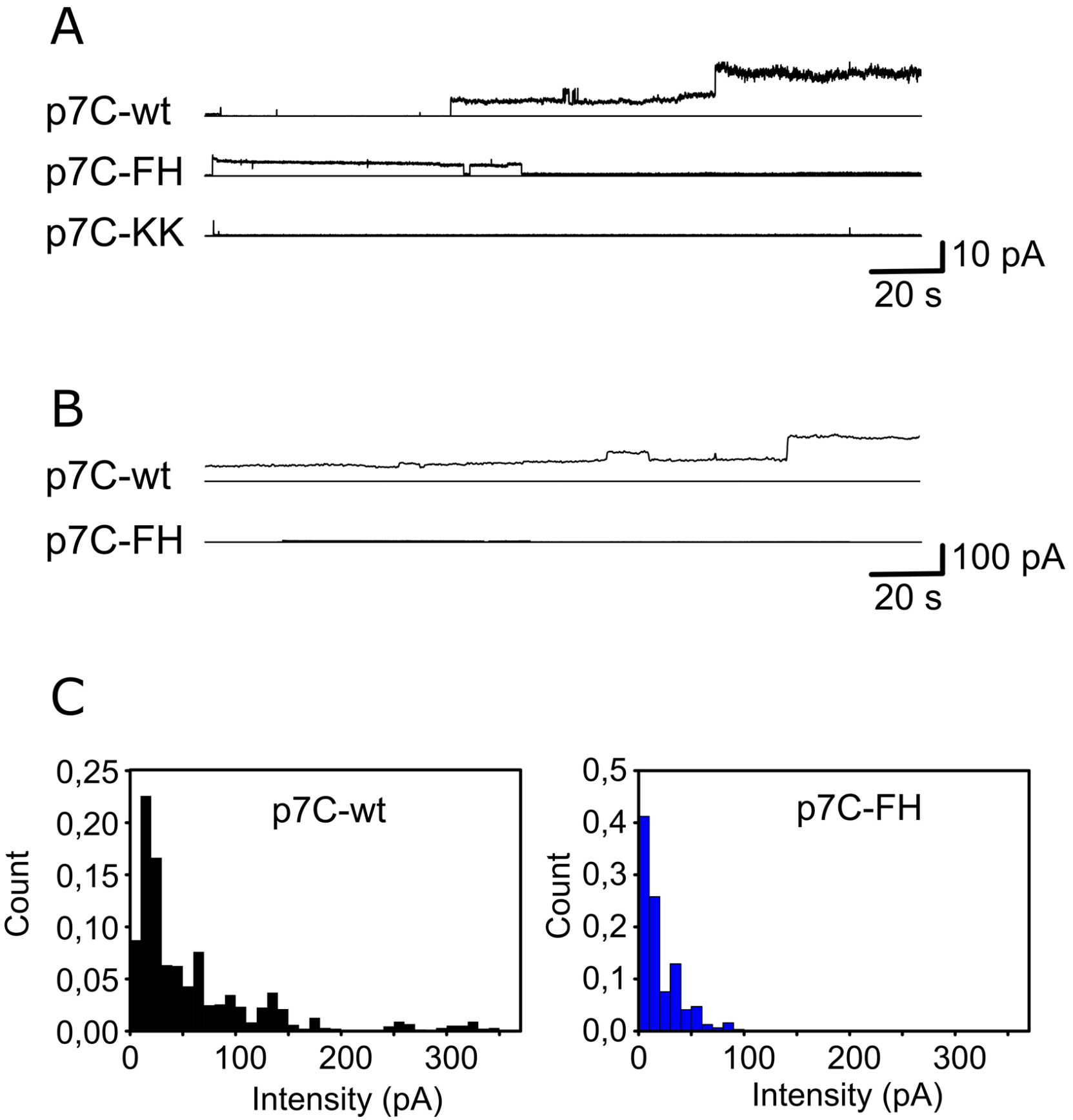
A
p7C-wt
p7C-FH
p7C-KK
10 pA
20 s
B
p7C-wt
p7C-FH
100 pA
20 s
C
p7C-wt
Count
0,25
0,20
0,15
0,10
0,05
0,00
0
100
200
300
Intensity (pA)
p7C-FH
Count
0,5
0,4
0,3
0,2
0,1
0,0
0
100
200
300
Intensity (pA)

Figure 2

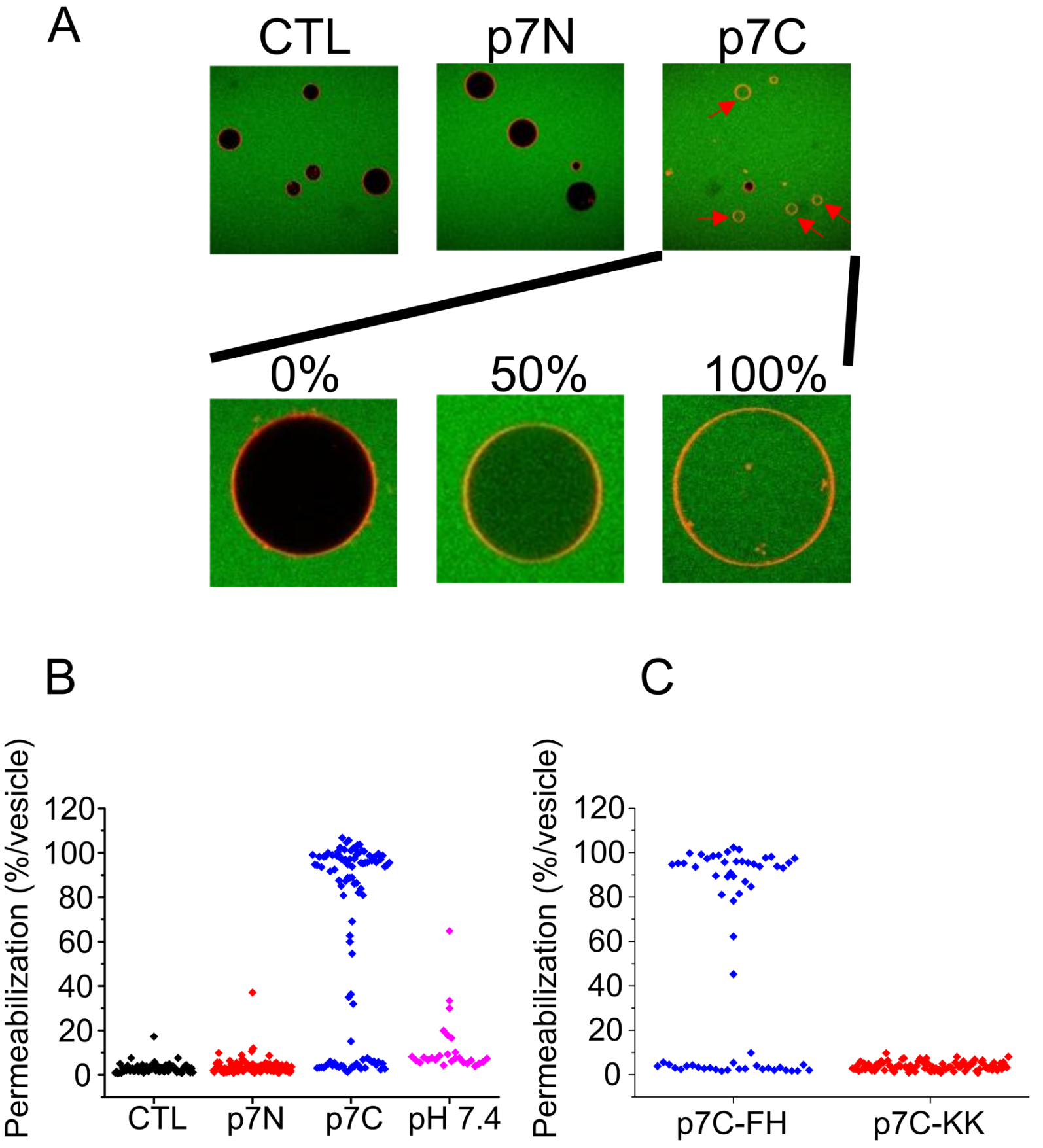
A
CTL
p7N
p7C
0%
50%
100%
B
Permeabilization (%/vesicle)
120
100
80
60
40
20
0
CTL
p7N
p7C
pH 7.4
C
Permeabilization (%/vesicle)
120
100
80
60
40
20
0
p7C-FH
p7C-KK

Figure 3

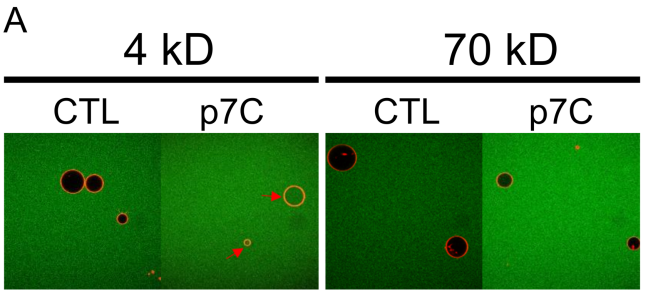
A
4 kD
70 kD
CTL
p7C
CTL
p7C

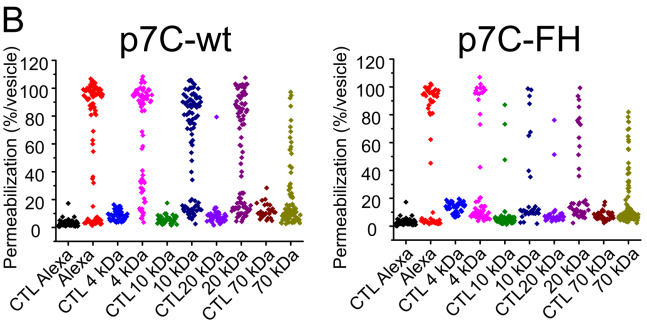
B
p7C-wt
p7C-FH
Permeabilization (%/vesicle)
0
20
40
60
80
100
120
CTL Alexa
Alexa
CTL 4 kDa
4 kDa
CTL 10 kDa
10 kDa
CTL 20 kDa
20 kDa
CTL 70 kDa
70 kDa

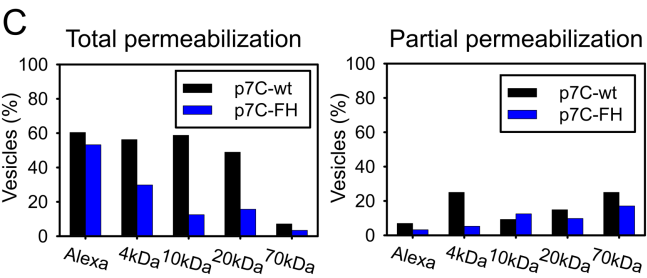
C
Total permeabilization
Partial permeabilization
Vesicles (%)
0
20
40
60
80
100
p7C-wt
p7C-FH
Alexa
4kDa
10kDa
20kDa
70kDa

Figure 4

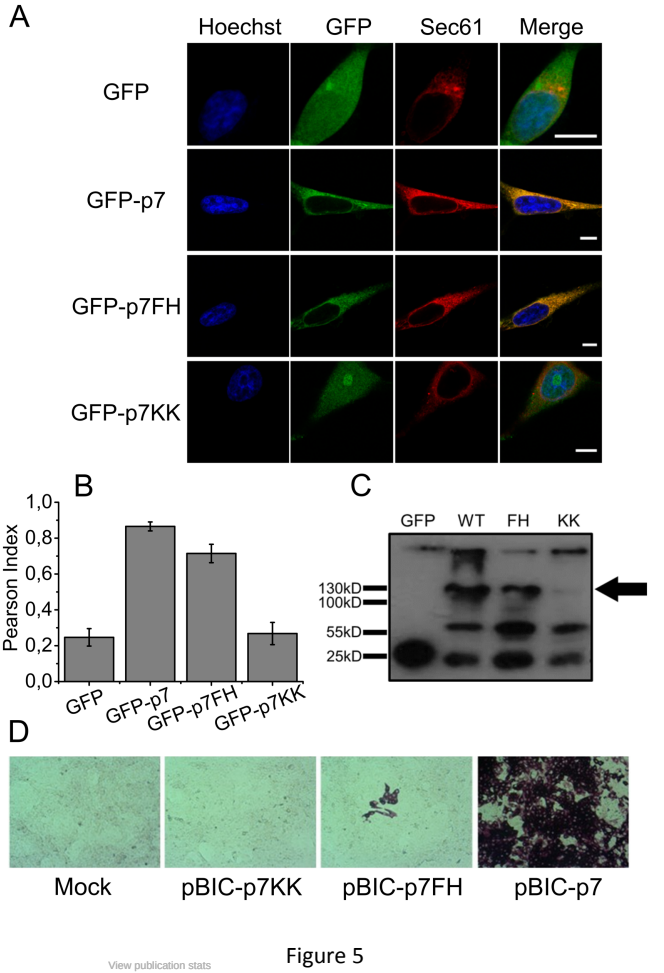


Figure 5